Original

Becherer, J.; Moum, J.; Calantoni, J.; Colosi, J.; Barth, J.; Lerczak, J.; McSweeney, J.; MacKinnnon, J.; Waterhouse, A.:
Saturation of the Internal Tide over the Inner Continental Shelf. Part I: Observations.
In: Journal of Physical Oceanography. Vol. 51 (2021) 8, 2553 - 2563.

First published online by AMS: 22.07.2021

https://dx.doi.org/10.1175/JPO-D-20-0264.1

Saturation of the Internal Tide over the Inner Continental Shelf. Part I: Observations

JOHANNES BECHERER,[a,b] JAMES N. MOUM,[a] JOSEPH CALANTONI,[c] JOHN A. COLOSI,[d] JOHN A. BARTH,[a] JAMES A. LERCZAK,[a] JACQUELINE M. MCSWEENEY,[a] JENNIFER A. MACKINNON,[e] AND AMY F. WATERHOUSE[e]

[a] *College of Earth, Ocean, and Atmospheric Sciences, Oregon State University, Corvallis, Oregon*
[b] *Helmholtz-Zentrum Hereon, Institute of Coastal Research, Geesthacht, Germany*
[c] *Ocean Sciences Division, U.S. Naval Research Laboratory, Stennis Space Center, Mississippi*
[d] *Department of Oceanography, Naval Postgraduate School, Monterey Bay, California*
[e] *Scripps Institution of Oceanography, University of California, San Diego, La Jolla, California*

(Manuscript received 22 October 2020, in final form 21 April 2021)

ABSTRACT: Broadly distributed measurements of velocity, density, and turbulence spanning the inner shelf off central California indicate that (i) the average shoreward-directed internal tide energy flux $\langle F_E \rangle$ decreases to near 0 at the 25-m isobath; (ii) the vertically integrated turbulence dissipation rate $\langle D \rangle$ is approximately equal to the flux divergence of internal tide energy $\partial_x \langle F_E \rangle$; (iii) the ratio of turbulence energy dissipation in the interior relative to the bottom boundary layer (BBL) decreases toward shallow waters; (iv) going inshore, $\langle F_E \rangle$ becomes decorrelated with the incoming internal wave energy flux; and (v) $\langle F_E \rangle$ becomes increasingly correlated with stratification toward shallower water.

SIGNIFICANCE STATEMENT: In addition to the well-known surface tide, there exists a tidal wave in the ocean's interior. This internal tide is considered important to ocean mixing and may propagate thousands of kilometers to its demise on continental shelves, where it ultimately breaks down through a hierarchy of complicated fluid dynamics. Now, with the aid of new sensors massively deployed over California's continental shelf, we have been able to determine that the energy lost to the shoaling internal tide goes almost completely to turbulence and is extinguished by the time it reaches the 25-m isobath. A surprising finding is that inshore of 50-m water depth the internal tide entirely loses memory of its initial strength.

KEYWORDS: Ocean; Continental shelf/slope; Coastal flows; Energy transport; Internal waves; Turbulence; Wave breaking

1. Introduction

The inner continental shelf is the region between surf zone and midcontinental shelf where surface and bottom boundary layers (BBL) converge or even overlap (Lentz 1994). Here, cross-shore winds contribute to transport across the inner shelf (Fewings et al. 2008), which over the mid shelf is driven by alongshore winds due to Ekman dynamics. Another, and previously uninvestigated, distinguishing feature of the inner shelf is as the region where the internal tide loses almost all of its energy. This latter aspect is our focus here and leads to a new distinction of the inner shelf's role as the surf zone for the internal tide (Becherer et al. 2021, hereafter Part II). This *internal* surf zone, in which the internal tide exists in a saturated state confined by the water depth, has features analogous to the surf zone for surface gravity waves (Thornton and Guza 1983; Battjes 1988).

The internal tide, generated either locally (Sharples et al. 2001; Duda and Rainville 2008; Kang and Fringer 2010) or at remote locations with long propagation path (Nash et al. 2012; Kumar et al. 2019), transmits a significant amount of energy onto the inner shelf (Moum et al. 2007b; Kang and Fringer 2012). Here that energy is dissipated by turbulence yielding diapycnal mixing and consequently water mass transformation. Over the inner shelf the internal tide plays a vital role in driving cross shelf transport of energy (Moum et al. 2007a), mass (Shroyer et al. 2010b), heat (Gough et al. 2020), nutrients (Sandstrom and Elliott 1984; Sharples et al. 2007), sediment (Butman et al. 2006; Pomar et al. 2012; Boegman and Stastna 2019; Becherer et al. 2020), and biomass (Scotti and Pineda 2007).

Understanding the cascade from low-frequency internal tide energy, that can originate many tens to thousands of kilometers away, including high-frequency nonlinear internal waves to small-scale turbulence and eventually mixing on the shelf has been the focus of several past studies (Helfrich and Melville 2006). These include idealized theoretical (e.g., Holloway et al. 1999; Grimshaw et al. 2004) and/or numerical studies (e.g., Vlasenko and Hutter 2002; Kang and Fringer 2010; Venayagamoorthy and Fringer 2007; Lamb 2014) as well as observations (e.g., Sherwin 1988; Sharples et al. 2001; Moum et al. 2007a; Shroyer et al. 2010a; Colosi et al. 2018).

The transformation from large-scale internal tide energy to small-scale dissipation and mixing on the shelf occurs through a hierarchy of mechanisms. As the internal tide approaches shallower waters it becomes increasingly nonlinear resulting in sharp bore fronts and/or the generation of higher-frequency wave trains (Henyey and Hoering 1997; Holloway et al. 2001; Apel 2003; Grimshaw et al. 2004; Scotti et al. 2008). These can generate turbulence due to bottom friction (Bogucki and Redekopp 1999; Stastna and Lamb 2002; Diamessis and Redekopp 2006; Allen et al. 2018; Becherer et al. 2020), strong interfacial shear (Bogucki and Garrett 1993; Sandstrom and Oakey 1995; Moum et al. 2003; Lamb and Farmer 2011), and

Corresponding author: Johannes Becherer, johannes.becherer@hereon.de

DOI: 10.1175/JPO-D-20-0264.1

more complicated breaking mechanisms (Vlasenko and Hutter 2002; Boegman and Ivey 2009; Aghsaee et al. 2010; Lamb 2014; Arthur and Fringer 2014). While understanding the mechanics of this hierarchy of processes is critical to the dissipation of the internal tide as it propagates onshore, we are interested here in the net sum of these mechanisms and consider the internal tide energy dissipation from a depth- and time-averaged perspective. In particular, we address the questions of where and how the energy of the incoming internal tide is distributed both vertically and horizontally over the inner shelf and how this varies according to governing environmental conditions. Leaving aside the details, we consider the onshore energy flux and turbulence dissipation (both in the interior and at the seafloor) to be due completely to the internal tide. We then compare measurements of onshore divergence of this flux to the measured turbulence dissipation. To this end we use an extensive dataset collected during a large 2-month-long experiment off the California coast (Lerczak et al. 2019; Kumar et al. 2021) including broadly distributed turbulence measurements from moored χpods (Moum and Nash 2009) and an array of >70 newly developed miniaturized turbulence measurement devices, termed GusT (Becherer et al. 2020), deployed on moorings and seafloor landers across and along the inner shelf (section 2).

In section 3c we show how the vertical distribution of turbulence changes across the shelf with increasing importance of BBL turbulence toward shallower waters. We find that the turbulence dissipation we measured on the shelf is roughly equal to the flux divergence of the internal tide (section 3b). The high correlation between incoming and local internal tide energy flux in deeper waters diminishes to near 0 in shallow waters. On the other hand, stratification is uncorrelated with internal tide energy flux in deeper waters but becomes increasingly correlated toward shallower waters (section 3d). While these correlations have been observed in previous studies (Colosi et al. 2018; Shroyer et al. 2011; Sharples and Zeldis 2019), dynamical explanation was not provided. In Part II, we use these observations to help in developing a parameterization for the cross-shelf dependence of the energy in the internal tide and then test this against a representative ensemble of published datasets.

2. Experiment

a. Study site

The data discussed in this manuscript originate from an experiment conducted off the coast of California off Point Sal in late summer/early fall of 2017 (Lerczak et al. 2019; Kumar et al. 2021). The study site is 50 km north of Point Conception, where cool waters from the California Current meet the warm waters from the Santa Barbara Channel.

Measurements at this site show the variability of near-coast temperature in different frequency bands (Feddersen et al. 2020). Subtidal variability is due to wind forcing and the associated up- and downwelling (Walter et al. 2017). During wind relaxations a plume of warm water from the Santa Barbara channel can travel up the coast to significantly change the temperature and stratification in the region (Washburn et al. 2011; Suanda et al. 2016). In the tidal band most variability is

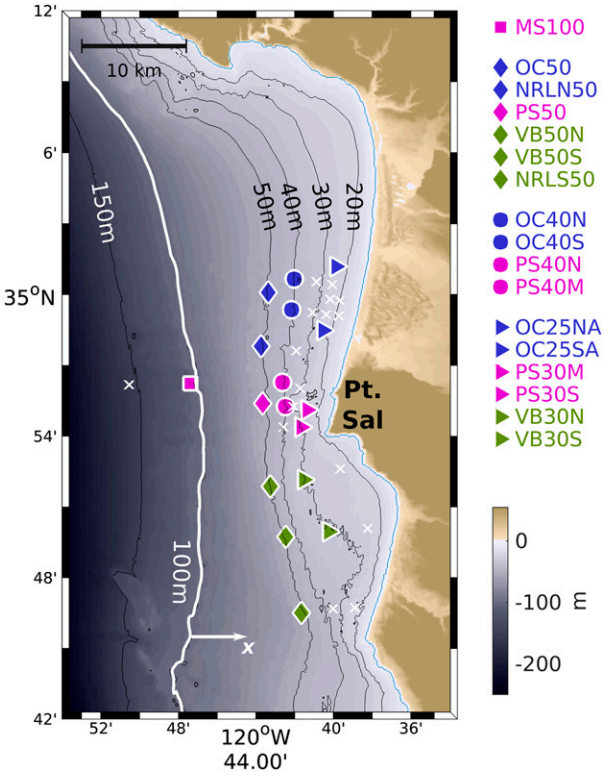

FIG. 1. Map of study site. Over 30 moorings were deployed at water depths deeper than 20 m during the ISDE, 17 of which provide a complete (or nearly complete) 2-month record in both temperature and velocity. These 17 moorings are grouped according to their depths into four categories (100, 50, 40, and <35 m). Based on their latitude we further distinguish three groups of moorings: north (blue), center (purple), and south (green). Mooring names are listed to the right of the map, where the number in the name indicates the deployment depth. The black contours on the map show 150-, 50-, 40-, 30-, and 20-m isobaths. The white contour marks the 100-m isobath, which is used as the zero reference for the x coordinate in this manuscript.

connected with the shoaling internal tide (Suanda et al. 2017; Colosi et al. 2018; McSweeney et al. 2020b). Strong tidal bores irregularly appear every 6–12 h, potentially indicating two or more local and/or nonlocal generation sites (McSweeney et al. 2020b). Here the continental shelf slope remains subcritical up to 100 km off the coast, which suggests an elevated importance of nonlocal internal tide generation (Kumar et al. 2019). In deep waters ($H > 40$ m) the internal tide appears coherent over tens of kilometers along the coast, but with decreasing coherence length scale toward shallowing depths (McSweeney et al. 2020a).

b. Field campaign

From September to November 2017 a large field campaign, the Inner Shelf Dynamics Experiment (ISDE), was conducted off Point Sal (Lerczak et al. 2019; Kumar et al. 2021). This experiment included more than 100 moorings deployed between 9 and 150 m of water depth (Lerczak et al. 2019; McSweeney et al. 2020a,b; Feddersen et al. 2020) as shown in Fig. 1, ship-based observations from three large vessels and

TABLE 1. Mooring table. The last column shows the mounting height (m above bottom) of all GusTs and χpods. Entries in parentheses correspond to χpods. In contrast to GusTs, χpods have two different FP07 sensors, which are both listed here. Moorings marked by * have been redeployed at the beginning of October 2017 with a refurbished set of turbulence sensors.

Mooring	Water depth (m)	Lon (°)	Lat (°)	(χpods), T-chain GusTs (m above bottom)
MS100	100	−120.79	34.94	85.0–75.0–64.0–(49.5–48.5)–28.0
*				82.5–77.5–72.5–63.0–62.0–(47.5–46.5)–28.0–13.0
OC-Array				
OC50	50	−120.72	35.00	37.5–30.0–26.5–21.5–16.5
*				36.5–30.0–26.0–21.5–16.0
OC40N	40	−120.70	35.01	25.5–17.0–10.5–4.5
*				25.5–17.0–4.5
OC40S	40	−120.70	34.99	25.0–20.0–15.0–10.0–5.0
*				25.0–20.0–15.0–10.0–5.0
OC25NA	25	−120.66	35.02	9.5
*				
OC25SA	25	−120.68	34.97	13.0–5.0–3.0
PS-Array				
PS50	50	−120.73	34.92	(5.5–4.5)
PS40N	40	−120.71	34.94	(6.0–5.0)
PS40M	40	−120.71	34.92	(6.0–5.0)
PS30M	27	−120.69	34.92	6.5
PS30S	30	−120.69	34.91	4.0
VB-Array				
VB50N	50	−120.72	34.86	5.5
VB50S	50	−120.71	34.83	37.5–27.5
VB30N	30	−120.69	34.87	3.0
VB30S	30	−120.67	34.83	15.0–10.0
NRL-Array				
NRLS50	50	−120.69	34.78	—
NRLN50	50	−120.73	34.96	—

four small boats, several drifter deployments (Spydell et al. 2019), four land-based and two ship-based X-band radars (Haller et al. 2019; E. Terrill et al. 2021, unpublished manuscript; Celona et al. 2021), airborne (Lenain et al. 2019) and satellite observations, and numerical modeling (Suanda et al. 2017; Kumar et al. 2019).

c. *Mooring setup*

During the two-month deployment, density was clearly dominated by temperature, such that salinity variations can be ignored (McSweeney et al. 2020b). Here, density was determined from moored temperature measurements alone (1–2-m spacing). Collocated with these temperature moorings were landers equipped with acoustic Doppler current meters (ADCPs) that provide full-depth velocity profiles. For details on the mooring setup see Lerczak et al. (2019) and McSweeney et al. (2020b). In this study we use only data from moorings deployed in water depths ≥ 25 m (Fig. 1; Table 1). Farther inshore surface wave contamination did not allow for reliable turbulence measurements.

d. *Turbulence measurements*

1) GUST: A NEW TURBULENCE MEASUREMENT DEVICE

A new, small, lightweight, low power turbulence measurement device was conceived specifically for the ISDE. The objective was to provide a component that might be suitable for deployment on a range of platforms, including moorings and towed bodies. Termed GusT and pronounced "gusty," this was developed through laboratory, wave tank, and field measurements, and 80 units were built for the experiment. They sample all signals continuously for up to 45 days at 100 Hz.

The GusT is equipped with a compass, a pressure sensor, three-component accelerometers, a fast-response thermistor (FP07) and a pitot-static tube. The pitot-static tube measures mean speed as well as velocity fluctuations, from which is inferred turbulent dissipation rates ε_p (Moum 2015; Becherer and Moum 2017; Becherer et al. 2020). In addition, we use the fast thermistor to estimate χ, the temperature variance dissipation rate, and from χ indirectly the turbulent kinetic energy dissipation rate ε_χ (Moum and Nash 2009; Becherer and Moum 2017).

The measurements from the fast thermistor and the pitot-static tube provide independent estimates of ε. In practice, these two estimates complement each other. In the well-mixed near-bottom region stratification is too small to estimate ε_χ reliably, but the near-bottom landers provide a very stable platform for GusTs from which to estimate ε_p from pitot-static tubes (Becherer et al. 2020). On the other hand, motion contamination causes problems with pitot-tube estimates on mooring lines, but sufficient stratification in the interior allows for thermistor-based estimates of ε_χ.

GusTs were deployed on a number of platforms during the experiment. While the majority of GusTs (>70) were on

moored T-chains and bottom landers, we also used GusTs on a tow-yo CTD, an instrumented bow chain, and a towed platform with CTD (Kumar et al. 2021).

2) Water column turbulence

Our estimate of vertically integrated energy dissipated in the water column includes contributions from the interior (D_{int}) and from the BBL (D_{bbl}).

Mid-water-column turbulence data used for this analysis comes from 60+ GusTs and six χpods (Moum and Nash 2009) deployed on moorings across the array. Table 1 lists all moorings with mounting depths for GusTs/χpods used in this paper. Note that no GusT was mounted closer than 12 m to the surface, a restriction determined by the depth of the principal buoyancy element (10 m) for each mooring.

From mid-water-column dissipation measurements using the method based on fast thermistors (Moum and Nash 2009; Becherer and Moum 2017), the depth-integrated dissipation rate from n GusTs/χpods at each mooring (excluding GusTs in the BBL) is

$$D_{\text{int}} = \rho_0 (H - h_{\text{bbl}}) \frac{1}{n} \sum_{i=1}^{n} \varepsilon_\chi^i \,(\text{W m}^{-2}) \tag{1}$$

$\rho_0 = 1025\,\text{kg m}^{-3}$ is a reference density, H the total water depth, and h_{bbl} the BBL height. Note that due to our sparse measurements we decided to use a simple unweighted instrument average in (1). While this approach could potentially yield local biases, our hope is that D_{int} still provides a good representation of shelf-wide averages.

3) Bottom boundary layer dissipation

Not all GusT deployments on landers provided a sufficiently long (at least 1 month) turbulence record for the array-wide analysis intended in this manuscript. Where and when GusT estimates of ε were not available, we follow Becherer et al. (2020) who showed that on time scales longer than 5 min, GusT's pitot-static tube estimates of ε_p are consistent with log-layer scaling

$$\varepsilon_{\text{bbl}} = \frac{u_*^3}{\kappa z} (\text{W kg}^{-1}), \tag{2}$$

where friction velocity is u_*, von Kármán's constant $\kappa = 0.4$, and the distance to the bed z. The friction velocity is estimated through a quadratic drag law from the speed measured at the lowermost bin of the lander-mounted ADCP, $u_*^2 = C_d u^2$. This yields estimates of ε_{bbl} from >15 bottom lander-mounted ADCPs with complete (experiment long) datasets thus adding indirect estimates to our array-wide turbulence analysis (Table 1).

The depth-dependent drag coefficient C_d is inferred from a best fit of (2) to direct turbulence measurements from the GusT, ε_p, mounted on the lander at OC50 (Fig. 2) that provides the longest continuous record of ε_p (Becherer et al. 2020). For different ADCPs the lower most bin is at different heights ranging from 1.5 to 6.5 m above the bottom. Therefore we cannot use the same drag coefficient in (2) at all locations. Rather we assume a constant roughness length parameter $z_0 = 1.2 \times 10^{-3}$ m (Becherer et al. 2020) that is then used to estimate the depth-dependent drag coefficient,

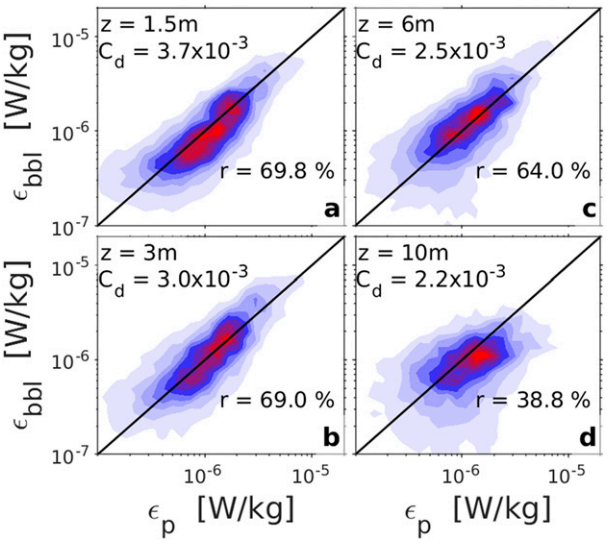

FIG. 2. Comparison between dissipation rates of BBL scaling using (2) from ADCP bins at different depth, ε_{bbl}, and direct measurements from the pitot-static tube, ε_p, at OC50. Note that C_d is different for every depth following (3).

$$C_d(z) = \kappa^2 \ln^{-2}\left(\frac{z}{z_0}\right). \tag{3}$$

Equivalently, we could have rescaled the velocity to a nominal height above the seafloor and applied a fixed drag coefficient, as is done in bulk flux estimates in the marine boundary layer (Fairall et al. 2003).

To calculate the energy dissipated vertically throughout the BBL (D_{bbl}) we integrate (2) over the log layer, which roughly spans $z = 20z_0 - h_{\text{bbl}}$ (Hinze 1975),

$$D_{\text{bbl}} = \frac{\rho_0 u_*^3}{\kappa} \overbrace{\int_{20z_0}^{h_{\text{bbl}}} \frac{1}{z} dz}^{I_{\text{bbl}}} (\text{W m}^{-2}). \tag{4}$$

The integral I_{bbl} ranges from 3.75 to 6 for $h_{\text{bbl}} = 1$–10 m. Since we do not typically have a good measure of h_{bbl} we assume here that it has a value of 5 m and make $I_{\text{bbl}} = 5$, with a corresponding ± 30% uncertainty in D_{bbl}. Note, that we ignore stratification in (4), which is accounted for by a modified log-layer scaling (Perlin et al. 2005), which leads to a correction that increases D_{bbl} by <30%, within the margin of error associated with our uncertainty in h_{bbl}. For simplicity, we use the unstratified log-layer scaling (2).

Combining the water column (1) and BBL measure (4) yields the full water column depth-integrated dissipation rate,

$$D = D_{\text{int}} + D_{\text{bbl}}. \tag{5}$$

3. Results

a. *Different internal responses to the shoaling internal tide*

McSweeney et al. (2020b) demonstrated that most of the variability in temperature and velocity at our site is connected

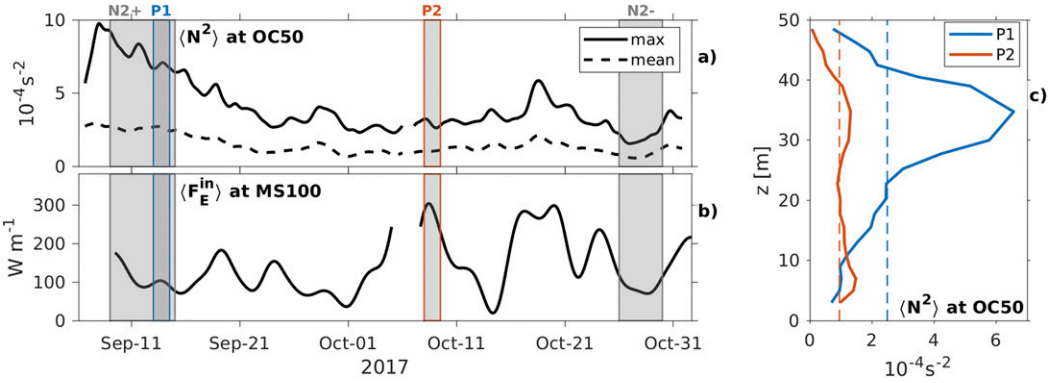

FIG. 3. Stratification and internal tidal energy flux conditions during the ISDE. (a) $\langle N^2 \rangle$ at OC50; water column maximum (solid) and mean (dashed line). (b) Incoming baroclinic energy flux $\langle F_E^{\text{in}} \rangle$, defined as the value of $\langle F_E \rangle$ [Eq. (7)] estimated at MS100. (c) Vertical profile of $\langle N^2 \rangle$ at OC50 averaged over the two periods marked as P1 and P2 in (a), where dashed lines indicate the depth means. The highlighted periods in (a) N2+, N2− correspond to dashed and dotted lines in Figs. 7c,d.

to internal tide forcing during the observation period from Sep to Nov 2017. This is consistent with a pilot study conducted 2 years earlier at the same site (Colosi et al. 2018).

In our record, internal tides are prominently visible at all mooring sites deeper than 20-m water depth. To illustrate this we examine the conditions at four moorings in different water depths during two brief periods representing different internal tide energy levels and stratification (Fig. 3). The first period represents weak to moderate internal tide energy levels with strong vertical stratification (blue box, P1, in Fig. 3a), and the second, strong internal-tidal forcing with weak to moderate stratification (orange box, P2).

During both P1 and P2 the internal tide is seen as large isopycnal displacements of tens of meters at intervals between 6 and 12 h (see also McSweeney et al. 2020b). The onshore velocity and isopycnal displacement show a clear mode one structure (Figs. 4, 5).

The amplitudes of both isopycnal displacements and velocities were smaller during P1 than P2, when displacements at OC50 and OC40 exceeded 75% of the water column (Fig. 5b,c). At MS100 and OC50, velocity amplitudes exceeded $0.3\,\text{m}\,\text{s}^{-1}$ during P2, compared to values $< 0.2\,\text{m}\,\text{s}^{-1}$ during P1 (cf. Figs. 4a,b and 5a,b).

In the mid–water column we observed many episodic events with dissipation rates up to $\varepsilon_\chi = 10^{-6}\,\text{m}^2\,\text{s}^{-1}$, shortly after or during large isopycnal displacements by the internal tide (Figs. 4, 5). These values are several orders of magnitude larger than typical values in the absence of tidally forced isopycnal displacements. The ε_{bbl} is controlled by near bottom currents, peak values of which typically occurred as part of a mode one vertical expression of steep internal tidal fronts (in the form of internal bores, e.g., 1000 UTC 8 October; Fig. 5a).

Profiles of $\langle \varepsilon \rangle$ averaged in time over P1 and P2 are shown in Figs. 4 and 5e–h. BBL values of dissipation $\langle \varepsilon_{\text{bbl}} \rangle$ were generally an order of magnitude larger than in the interior $\langle \varepsilon_\chi \rangle$. Throughout the water column, values of $\langle \varepsilon \rangle$ were significantly greater during P2 than P1 Fig. 4e–h, associating stronger internal tidal forcing with greater turbulence energy losses.

b. *Shelf-wide energy flux and dissipation*

The examples in Figs. 4, 5 suggest that turbulence over the inner shelf is strongly linked to internal tidal forcing. To study this connection quantitatively we start with a depth-integrated energy balance

$$\partial_t E = \nabla \cdot (F_E + F_E^{\text{nl}}) - D + \text{source} \tag{6}$$

where $\partial_t E$ is the rate of change of the depth-integrated internal wave energy, and $\nabla \cdot (F_E + F_E^{\text{nl}})$ the divergence of the linear (F_E) and nonlinear (F_E^{nl}) components of the flux and the last term represents other possible sources and sinks.

We estimate F_E at all mooring sites (see Fig. 1) with complete records of both temperature and velocity for the entirety of the 2-month deployment. The F_E is estimated following Nash et al. (2005)

$$F_E = \int_0^H u' p'\, dz \tag{7}$$

where $u' = u - \langle u \rangle - \overline{u} + \overline{\langle u \rangle}$ and $p' = p_s + g\int_z^H \rho'\, d\tilde{z}$ with $\langle \cdot \rangle$ representing a 36-h low-pass filter and $\bar{\cdot}$ the vertical mean. The surface pressure p_s was calculated indirectly with the condition $\int p'\, dz = 0$. The density perturbation is $\rho' = \rho - \langle \rho \rangle$.

For individual high-frequency nonlinear internal waves Moum et al. (2007b) showed that F_E^{nl} is of the same order as F_E. However, Nash et al. (2012) showed that nonlinear fluxes are typically much smaller than the linear flux for the low-frequency component of the internal tide. In a tidally averaged sense, our estimates of $\langle F_E^{\text{nl}} \rangle$ are typically one order of magnitude smaller than $\langle F_E \rangle$ with variable sign (not shown). We proceed by neglecting F_E^{nl}.

While F_E fluctuates on short time scales (Fig. 6), $\langle F_E \rangle$ is consistently positive (shoreward directed) at all mooring sites. Figure 7a shows values averaged over the entire length of the experiment (2 month), $\langle F_E \rangle_{\text{ex}}$, at each mooring location as a function of cross-shelf distance x, where the x axis corresponds to distance from the 100-m isobath, with x increasing shoreward.

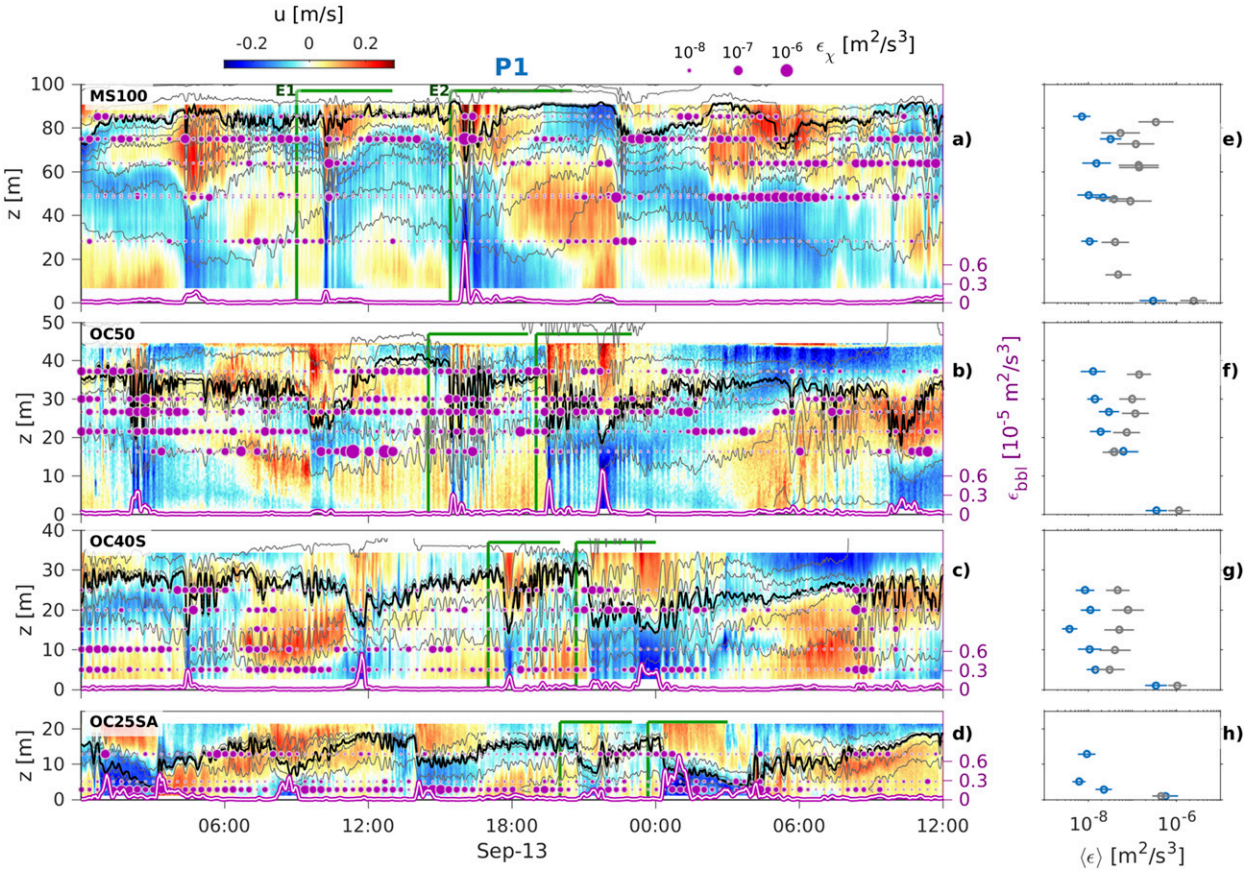

FIG. 4. Dissipation of the internal tide between the 25-m and 100-m isobaths. (a)–(d) Cross-shore velocity [red (blue) colors on- (off)-shore directed] during period P1 (see Fig. 3a) at four isobaths in the same general area; temperature is represented by gray contours 10–20°C at 1° increments; the black line indicates the pycnocline (N^2_{max}); purple dots show the magnitude of ε_χ measured in the interior with GusTs and χpods, scaled according to the legend atop (a); and the purple/white line is ε_{bbl}, obtained from BBL scaling of near-bottom ADCP bins. (e)–(h) Time-averaged $\langle\varepsilon\rangle$ profiles for P1 (blue) and P2 (gray), respectively. To show the evolution of the internal tide over the inner shelf, we mark two arbitrary wave events, E1 and E2, with green overbars at each mooring site. These two examples are portrayed in spatial domain in Figs. 1a and 1b of Part II.

From MS100 ($x = 0$ km) to OC25NA ($x \approx 13$ km) $\langle F_E\rangle_{ex}$ decreases by almost two orders of magnitude from more than 100 to about 3 W m^{-1} (Fig. 7a). This indicates that a major fraction of the internal tide energy is lost between the 100- and the 25-m isobath. An exponential fit with the general form $y = \exp(ax^2 + bx + c)$ matches the values in Fig. 7a (black line).

The slope of the fitted line in Fig. 7a represents the cross-shelf component of the flux divergence of the internal tide ($\langle\partial_x F_E\rangle_{ex}$, black line in Fig. 7b). A comparison of $\langle\partial_x F_E\rangle_{ex}$ (black) and $\langle D\rangle_{ex}$ (symbols + corresponding fit in red) in Fig. 7b suggest that a large fraction of the dissipation we measure can be accounted for by the flux divergence of the internal tide. Indirectly, this also suggests that our measurements capture most of the energy dissipation over the shelf and that the rate of change term in (6) is relatively small. Depth-integrated and time-averaged dissipation rates, $\langle D\rangle_{ex}$, range from about 0.01 W m^{-2} at deep sites to about 0.002 W m^{-2} in shallow water. Cross-shelf peak values of $\langle D\rangle_{ex}$ cluster near the 50-m isobath (Fig. 7b).

c. *Relative importance of D_{int} and D_{bbl}*

At all locations, dissipation in the BBL exceeds dissipation in the interior. The ratio $\langle D_{int}\rangle_{ex}/\langle D_{bbl}\rangle_{ex}$ generally decreases with decreasing water depth (Fig. 8). At MS100 $\langle D_{int}\rangle_{ex}/\langle D_{bbl}\rangle_{ex} \approx 0.45$, and decreases inshore. At OC25NA roughly 5% of $\langle D\rangle_{ex}$ occurs in the interior.

This is largely consistent with previous studies that found that BBL dynamics play a leading role in dissipating internal tidal energy on the shelf (Inall et al. 2000; Rippeth and Inall 2002).

It is important to note here that all of our dissipation measurements are deeper than 12 m (see Table 1), which excludes the contributions from the upper water column. In the sense that this reduces the compounding influence of surface forcing, this might be considered a positive effect in isolating the influence of the internal tide.

d. *Dependence on environmental conditions*

Figure 7d illustrates that both the magnitudes and cross-shelf slopes of $\langle\partial_x F_E\rangle$ (black) and $\langle D\rangle$ are variable. During

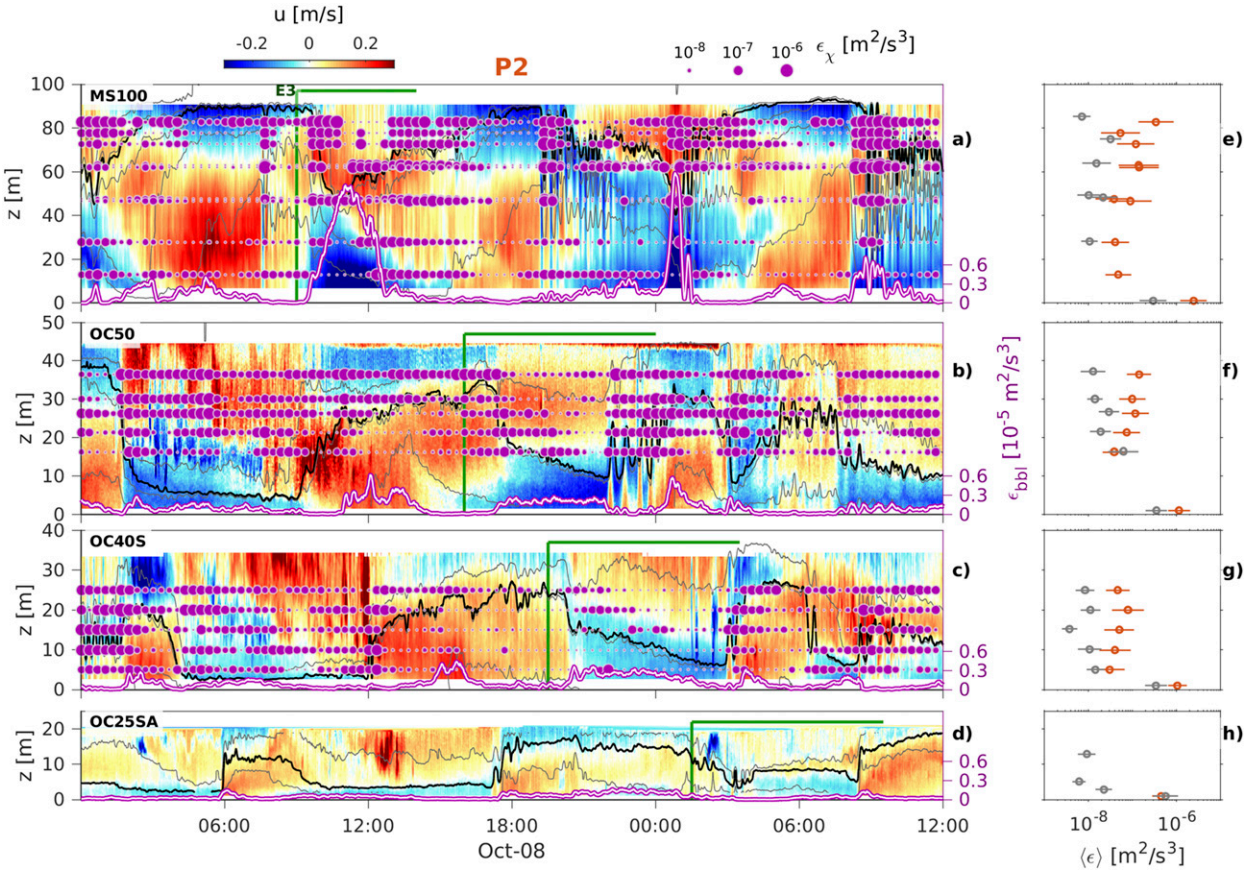

FIG. 5. As in Fig. 4, but for period P2 (see Fig. 3a). In (e)–(h) time-averaged $\langle\varepsilon\rangle$ profiles for P2 are in red, and corresponding values for P1 are given in gray as reference. Green marks in (a)–(d) correspond to event E3 illustrated in Fig. 1c of Part II.

periods of strong shelf stratification (N2+ in Fig. 3a) the slope of $\langle F_E\rangle$ was relatively small such that a significant portion of the energy of the internal tide is fluxed to shallower sites (dashed line Figs. 7c,d). On the other hand during weak stratification (N2− in Fig. 3a), $\langle F_E\rangle$ decreased more steeply toward shore and almost all energy is lost offshore of the 25-m isobath (dotted line Figs. 7c,d).

To study how $\langle F_E\rangle$ changes due to environmental conditions we first look at the incoming tidal energy. The internal tide is generated at the shelf break and/or at remote locations by extracting energy from the barotropic tide. Nash et al. (2012) demonstrated that remotely generated tides can have a substantial influence on the shoreward baroclinic energy flux, both due to direct contribution as well as indirect interference with the locally generated tide. This influence can even yield situations where the onshore baroclinic energy flux is entirely out of synchronization with the neap–spring cycle. From a model study of the study site, Kumar et al. (2019) showed that generation sites $O(100)$ km away are likely more important for the internal tide signal than local shelf break generation.

To test the dependence of the distribution of $\langle F_E\rangle$ across the inner shelf on the incoming internal-tidal energy levels, we use the baroclinic energy flux measured at MS100 as a reference and define it as the incoming flux $\langle F_E^{\text{in}}\rangle$. In Fig. 9a we show the correlation between $\langle F_E\rangle$ and $\langle F_E^{\text{in}}\rangle$. The correlation decreases toward shore, tending to 0 at the shallowest sites. This is a surprising finding, implying that internal tide energy in shallow waters is unrelated to the incoming flux $\langle F_E^{\text{in}}\rangle$. Apparently the internal tide loses memory of its generation as it shoals.

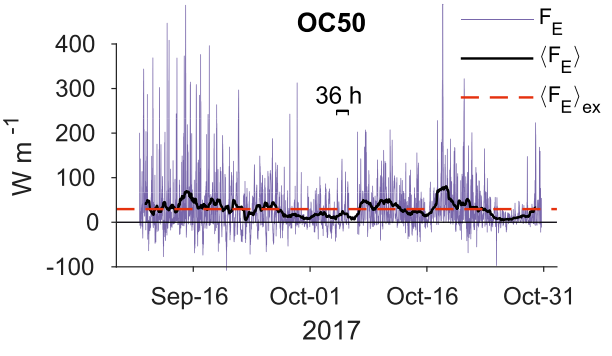

FIG. 6. Onshore component of the depth-integrated internal wave energy flux at mooring OC50. Instantaneous flux F_E (blue), calculated with (7), 36-h moving average $\langle F_E\rangle$ (black), and experiment long average $\langle F_E\rangle_{ex}$ (red dashed). The filter length (36 h) for $\langle F_E\rangle$ is indicated in the middle of the panel.

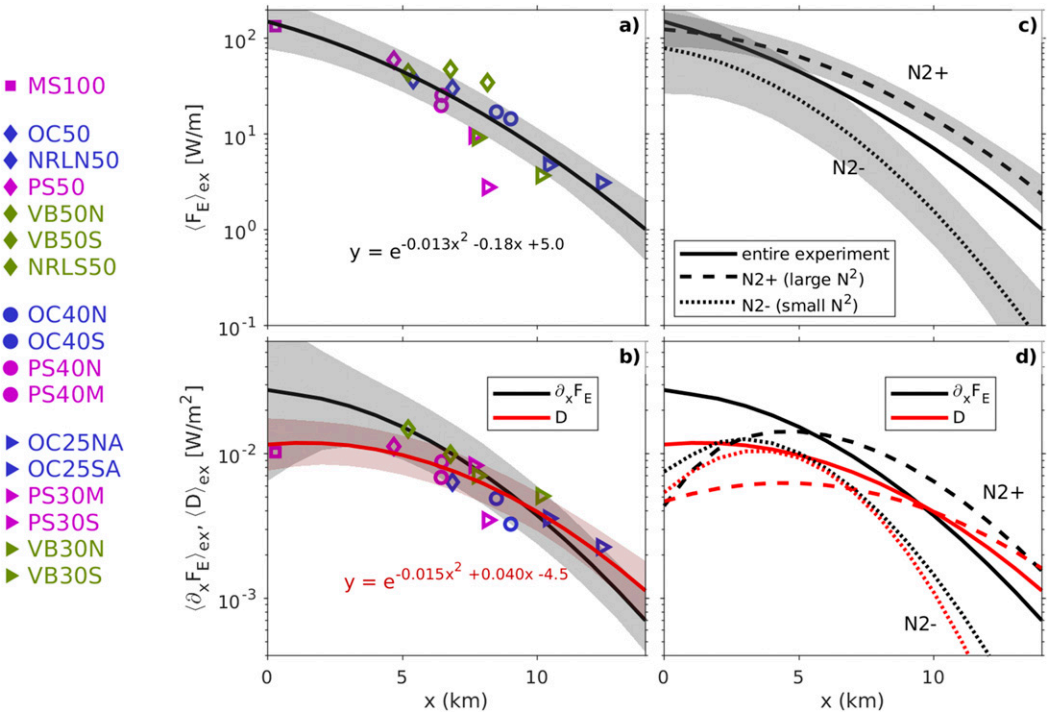

FIG. 7. (a) Onshore component of baroclinic energy flux averaged over the entire deployment period $\langle F_E \rangle_{ex}$ at each mooring. The black line shows a best fit of the form $y = \exp(ax^2 + bx + c)$. (b) $\langle D \rangle_{ex}$ (symbols and best fit, red line) and $\langle \partial_x F_E \rangle_{ex}$ [black line as estimated from the fit in (a)]. (c) Comparison of best fits as in (a) for the entire deployment period (solid), a strong (dashed, N2+) and a weak (dotted, N2−) stratification period corresponding to gray shaded times in Fig. 3a. (d) Fits as in (b) contrasting the entire deployment (solid) to N2+ (dashed) and N2− (dotted), respectively. The x axis is distance from the 100-m isobath (white line in Fig. 1), with x increasing toward shore. Shaded areas in (a), (b), and (c) correspond to 68% confidence intervals for the respective fit.

The correlation between mean shelf stratification $\langle \overline{N^2} \rangle$ and $\langle F_E \rangle$ has an opposite cross-shelf behavior (Fig. 9b). At deep sites the correlation is weak to nonexistent (at MS100 $r^2 \approx 0$). The correlation increases shoreward to $r^2 \approx 0.8$ at OC25SA. This suggests that stratification controls how much internal tide energy can be transported across the inner shelf. When stratification is weak the internal tide dissipates more of its energy farther offshore; under stronger stratification a greater portion of energy reaches the shallowest sites.

To better understand this surprising dependence, we introduce the concept of a *saturated internal tide* in Part II, and then determine how well this concept explains the dependencies noted above.

4. Conclusions

From a unique dataset with broadly distributed velocity, density and, notably, turbulence measurements spanning the inner continental shelf off central California, we make several key observations related to the evolution of the internal tide as it progresses shoreward:

- the shoreward-directed energy fluxed by the internal tide $\langle F_E \rangle$ decreases from near 100 W m^{-1} at the 100-m isobath to near 0 at 25 m (Fig. 7);
- the vertically integrated turbulence dissipation rate $\langle D \rangle$ is approximately equal to the divergence of the flux of internal tide energy $\partial_x \langle F_E \rangle$ (Fig. 7b);

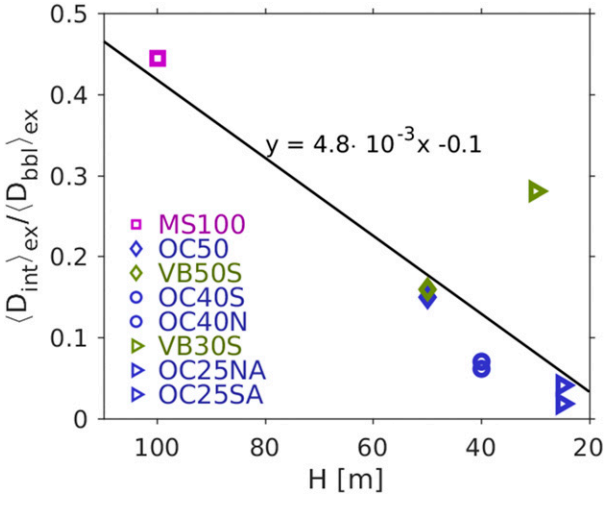

FIG. 8. Ratio of $\langle D_{int} \rangle_{ex}$ to $\langle D_{bbl} \rangle_{ex}$ as a function of total water depth H. Note that only moorings are considered here that had at least two GusTs mounted at different depths (see Table 1).

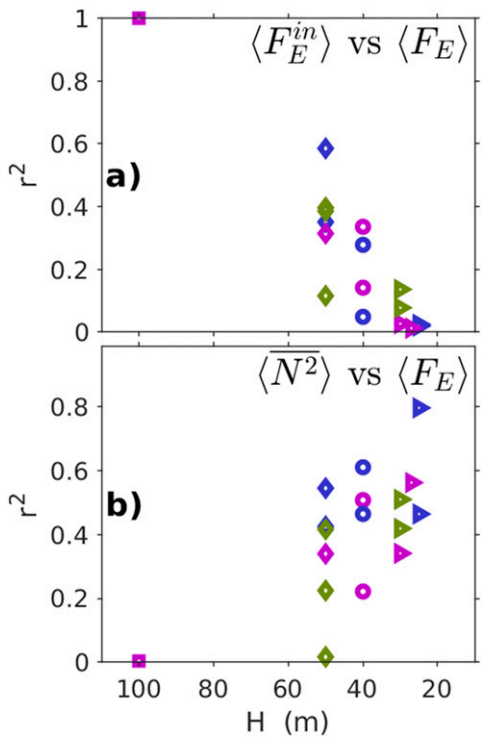

FIG. 9. Correlation between the baroclinic energy flux $\langle F_E \rangle$ at each mooring and (a) the incoming flux $\langle F_E^{\text{in}} \rangle$, measured at MS100 and (b) vertically averaged stratification $\langle \overline{N^2} \rangle$ for each mooring. The correlation r^2 was calculated on 36-h low-pass-filtered time series.

- the rate of turbulence energy dissipated in the interior relative to that in BBL ($\langle D_{\text{int}} \rangle / \langle D_{\text{bbl}} \rangle$) decreases toward shallow waters (Fig. 8);
- toward shallow water, $\langle F_E \rangle$ becomes decorrelated with the incoming energy flux ($\langle F_E^{\text{in}} \rangle$) measured at the 100-m isobath (Fig. 9a). That is, the internal tide loses memory of its initial strength as it shoals; and
- while $\langle F_E \rangle$ is uncorrelated with $\langle \overline{N^2} \rangle$ at the 100-m isobath, these become increasingly correlated toward shallower water (Fig. 9b).

Our broad brush approach to assessing the energy flux and dissipation of the internal tide sets aside the details of bore steepening, solitary wave fission, breaking, among many others. It also may include energy and dissipation that is incorrectly assigned to the internal tide. It resolves neither the complete onshore evolution nor the along-shelf variations. Yet it provides a consistent and intriguing correspondence between $\partial_x \langle F_E \rangle$ and $\langle D \rangle$. In Part II, we expand on this result to develop a simple parameterization for the cross-shelf dependencies of $\langle F_E \rangle$ and $\partial_x \langle F_E \rangle$, as well as available potential energy. Testing this parameterization against a range of published datasets suggests broad applicability and that the simplifying assumptions we have made in this analysis cannot be far wrong.

Acknowledgments. The work described here was fully funded by the Office of Naval Research through the Inner Shelf DRI. We acknowledge the efforts of Craig Van Appledorn, Pavan Vutukur, and Kerry Latham in building, testing, calibrating, and deploying GusTs. We thank the full host of participants for helping with deployments and for attempting to incorporate GusTs on their platforms, some of which were not well suited for such a device. We furthermore thank the crew members of R/V *Oceanus* and R/V *Sally Ride*. We thank Alexis Kaminski for her enthusiastic contribution in the field work and early data analysis. We are grateful to two anonymous reviewers and editor Jody Klymak for their time and valuable comments.

Data availability statement. All data used in this manuscript are achieved and publicly available under https://doi.org/10.6075/J0WD3Z3Q.

REFERENCES

Aghsaee, P., L. Boegman, and K. G. Lamb, 2010: Breaking of shoaling internal solitary waves. *J. Fluid Mech.*, **659**, 289–317, https://doi.org/10.1017/S002211201000248X.

Allen, R. M., J. A. Simeonov, J. Calantoni, M. T. Stacey, and E. A. Variano, 2018: Turbulence in the presence of internal waves in the bottom boundary layer of the california inner shelf. *Ocean Dyn.*, **68**, 627–644, https://doi.org/10.1007/s10236-018-1147-7.

Apel, J. R., 2003: A new analytical model for internal solitons in the ocean. *J. Phys. Oceanogr.*, **33**, 2247–2269, https://doi.org/10.1175/1520-0485(2003)033<2247:ANAMFI>2.0.CO;2.

Arthur, R. S., and O. B. Fringer, 2014: The dynamics of breaking internal solitary waves on slopes. *J. Fluid Mech.*, **761**, 360–398, https://doi.org/10.1017/jfm.2014.641.

Battjes, J., 1988: Surf-zone dynamics. *Annu. Rev. Fluid Mech.*, **20**, 257–291, https://doi.org/10.1146/annurev.fl.20.010188.001353.

Becherer, J., and J. N. Moum, 2017: An efficient scheme for onboard reduction of moored χpod data. *J. Atmos. Oceanic Technol.*, **34**, 2533–2546, https://doi.org/10.1175/JTECH-D-17-0118.1.

——, ——, J. A. Colosi, J. A. Lerczak, and J. M. McSweeney, 2020: Turbulence asymmetries in bottom boundary layer velocity pulses associated with onshore-propagating nonlinear internal waves. *J. Phys. Oceanogr.*, **50**, 2373–2391, https://doi.org/10.1175/JPO-D-19-0178.1.

——, and Coauthors, 2021: Saturation of the internal tide over the inner continental shelf. Part II: Parameterization. *J. Phys. Oceanogr.*, **51**, 2565–2582, https://doi.org/10.1175/JPO-D-21-0047.1.

Boegman, L., and G. N. Ivey, 2009: Flow separation and resuspension beneath shoaling nonlinear internal waves. *J. Geophys. Res.*, **114**, C02018, https://doi.org/10.1029/2007JC004411.

——, and M. Stastna, 2019: Sediment resuspension and transport by internal solitary waves. *Annu. Rev. Fluid Mech.*, **51**, 129–154, https://doi.org/10.1146/annurev-fluid-122316-045049.

Bogucki, D. J., and C. Garrett, 1993: A simple model for the shear-induced decay of an internal solitary wave. *J. Phys. Oceanogr.*, **23**, 1767–1776, https://doi.org/10.1175/1520-0485(1993)023<1767:ASMFTS>2.0.CO;2.

——, and L. G. Redekopp, 1999: A mechanism for sediment resuspension by internal solitary waves. *Geophys. Res. Lett.*, **26**, 1317–1320, https://doi.org/10.1029/1999GL900234.

Butman, B., P. Alexander, A. Scotti, R. Beardsley, and S. Anderson, 2006: Large internal waves in Massachusetts Bay transport sediments offshore. *Cont. Shelf Res.*, **26**, 2029–2049, https://doi.org/10.1016/j.csr.2006.07.022.

Celona, S., S. T. Merrifield, T. de Paolo, N. Kaslan, T. Cook, J. A. Colosi, and E. J. Terrill, 2021: Automated detection, classification, and tracking of internal wave signatures using X-band radar in the inner shelf. *J. Atmos. Oceanic Technol.*, **38**, 789–803, https://doi.org/10.1175/JTECH-D-20-0129.1.

Colosi, J. A., N. Kumar, S. H. Suanda, T. M. Freismuth, and J. H. MacMahan, 2018: Statistics of internal tide bores and internal solitary waves observed on the inner continental shelf off Point Sal, California. *J. Phys. Oceanogr.*, **48**, 123–143, https://doi.org/10.1175/JPO-D-17-0045.1.

Diamessis, P. J., and L. G. Redekopp, 2006: Numerical investigation of solitary internal wave-induced global instability in shallow water benthic boundary layers. *J. Phys. Oceanogr.*, **36**, 784–812, https://doi.org/10.1175/JPO2900.1.

Duda, T. F., and L. Rainville, 2008: Diurnal and semidiurnal internal tide energy flux at a continental slope in the South China Sea. *J. Geophys. Res.*, **113**, C03025, https://doi.org/10.1029/2007JC004418.

Fairall, C., E. Bradley, J. Hare, A. Grachev, and J. Edson, 2003: Bulk parameterization of air–sea fluxes: Updates and verification for the COARE algorithm. *J. Climate*, **16**, 571–591, https://doi.org/10.1175/1520-0442(2003)016<0571:BPOASF>2.0.CO;2.

Feddersen, F., J. H. MacMahan, T. M. Freismuth, M. K. Gough, and M. Kovatch, 2020: Inner shelf vertical and alongshore temperature variability in the subtidal, diurnal, and semidiurnal bands along the central California coastline with headlands. *J. Geophys. Res. Oceans*, **125**, e2019JC015347, https://doi.org/10.1029/2019JC015347.

Fewings, M., S. J. Lentz, and J. Fredericks, 2008: Observations of cross-shelf flow driven by cross-shelf winds on the inner continental shelf. *J. Phys. Oceanogr.*, **38**, 2358–2378, https://doi.org/10.1175/2008JPO3990.1.

Gough, M. K., T. M. Freismuth, J. H. MacMahan, J. A. Colosi, S. H. Suanda, and N. Kumar, 2020: Heating of the midshelf and inner shelf by warm internal tidal bores. *J. Phys. Oceanogr.*, **50**, 2609–2620, https://doi.org/10.1175/JPO-D-19-0143.1.

Grimshaw, R., E. Pelinovsky, T. Talipova, and A. Kurkin, 2004: Simulation of the transformation of internal solitary waves on oceanic shelves. *J. Phys. Oceanogr.*, **34**, 2774–2791, https://doi.org/10.1175/JPO2652.1.

Haller, M., D. Honegger, R. Pittman, A. O'Dea, and A. Simpson, 2019: Real-time marine radar observations of nearshore waves and flow structures from shore-based towers. *IEEE/OES Twelfth Current, Waves and Turbulence Measurement (CWTM)*, San Diego, CA, IEEE, 1–7, https://doi.org/10.1109/CWTM43797.2019.8955152.

Helfrich, K. R., and W. K. Melville, 2006: Long nonlinear internal waves. *Annu. Rev. Fluid Mech.*, **38**, 395–425, https://doi.org/10.1146/annurev.fluid.38.050304.092129.

Henyey, F. S., and A. Hoering, 1997: Energetics of borelike internal waves. *J. Geophys. Res.*, **102**, 3323–3330, https://doi.org/10.1029/96JC03558.

Hinze, J., 1975: *Turbulence.* 2nd ed. McGraw-Hill, Inc., 790 pp.

Holloway, P. E., E. Pelinovsky, and T. Talipova, 1999: A generalized Korteweg-de Vries model of internal tide transformation in the coastal zone. *J. Geophys. Res.*, **104**, 18 333–18 350, https://doi.org/10.1029/1999JC900144.

——, P. G. Chatwin, and P. Craig, 2001: Internal tide observations from the Australian north west shelf in summer 1995. *J. Phys. Oceanogr.*, **31**, 1182–1199, https://doi.org/10.1175/1520-0485(2001)031<1182:ITOFTA>2.0.CO;2.

Inall, M. E., T. P. Rippeth, and T. J. Sherwin, 2000: Impact of nonlinear waves on the dissipation of internal tidal energy at a shelf break. *J. Geophys. Res.*, **105**, 8687–8705, https://doi.org/10.1029/1999JC900299.

Kang, D., and O. Fringer, 2010: On the calculation of available potential energy in internal wave fields. *J. Phys. Oceanogr.*, **40**, 2539–2545, https://doi.org/10.1175/2010JPO4497.1.

——, and ——, 2012: Energetics of barotropic and baroclinic tides in the Monterey Bay area. *J. Phys. Oceanogr.*, **42**, 272–290, https://doi.org/10.1175/JPO-D-11-039.1.

Kumar, N., S. Suanda, J. Colosi, K. Haas, E. DiLorenzo, A. Miller, and C. Edwards, 2019: Coastal semidiurnal internal tidal incoherence in the Santa Maria Basin, California: Observations and model simulations. *J. Geophys. Res. Oceans*, **124**, 5158–5179, https://doi.org/10.1029/2018JC014891.

——, and Coauthors, 2021: The Inner-Shelf Dynamics Experiment. *Bull. Amer. Meteor. Soc.*, **102**, E1033–E1063, https://doi.org/10.1175/BAMS-D-19-0281.1.

Lamb, K. G., 2014: Internal wave breaking and dissipation mechanisms on the continental slope/shelf. *Annu. Rev. Fluid Mech.*, **46**, 231–254, https://doi.org/10.1146/annurev-fluid-011212-140701.

——, and D. Farmer, 2011: Instabilities in an internal solitary-like wave on the Oregon shelf. *J. Phys. Oceanogr.*, **41**, 67–87, https://doi.org/10.1175/2010JPO4308.1.

Lenain, L., N. M. Statom, and W. K. Melville, 2019: Airborne measurements of surface wind and slope statistics over the ocean. *J. Phys. Oceanogr.*, **49**, 2799–2814, https://doi.org/10.1175/JPO-D-19-0098.1.

Lentz, S. J., 1994: Current dynamics over the Northern California inner shelf. *J. Phys. Oceanogr.*, **24**, 2461–2478, https://doi.org/10.1175/1520-0485(1994)024<2461:CDOTNC>2.0.CO;2.

Lerczak, J., and Coauthors, 2019: Untangling a web of interactions where surf meets coastal ocean. *Eos, Trans. Amer. Geophys. Union*, **100**, https://doi.org/10.1029/2019EO122141.

McSweeney, J. M., and Coauthors, 2020a: Alongshore variability of shoaling internal bores on the inner shelf. *J. Phys. Oceanogr.*, **50**, 2965–2981, https://doi.org/10.1175/JPO-D-20-0090.1.

——, and Coauthors, 2020b: Observations of shoaling nonlinear internal bores across the central California inner shelf. *J. Phys. Oceanogr.*, **50**, 111–132, https://doi.org/10.1175/JPO-D-19-0125.1.

Moum, J. N., 2015: Ocean speed and turbulence measurements using pitot-static tubes on moorings. *J. Atmos. Oceanic Technol.*, **32**, 1400–1413, https://doi.org/10.1175/JTECH-D-14-00158.1.

——, and J. Nash, 2009: Mixing measurements on an equatorial ocean mooring. *J. Atmos. Oceanic Technol.*, **26**, 317–336, https://doi.org/10.1175/2008JTECHO617.1.

Moum, J., D. Farmer, W. Smyth, L. Armi, and S. Vagle, 2003: Structure and generation of turbulence at interfaces strained by internal solitary waves propagating shoreward over the continental shelf. *J. Phys. Oceanogr.*, **33**, 2093–2112, https://doi.org/10.1175/1520-0485(2003)033<2093:SAGOTA>2.0.CO;2.

Moum, J. N., D. Farmer, E. Shroyer, W. Smyth, and L. Armi, 2007a: Dissipative losses in nonlinear internal waves propagating across the continental shelf. *J. Phys. Oceanogr.*, **37**, 1989–1995, https://doi.org/10.1175/JPO3091.1.

——, J. Klymak, J. Nash, A. Perlin, and W. Smyth, 2007b: Energy transport by nonlinear internal waves. *J. Phys. Oceanogr.*, **37**, 1968–1988, https://doi.org/10.1175/JPO3094.1.

Nash, J. D., M. H. Alford, and E. Kunze, 2005: Estimating internal wave energy fluxes in the ocean. *J. Atmos. Oceanic Technol.*, **22**, 1551–1570, https://doi.org/10.1175/JTECH1784.1.

——, S. M. Kelly, E. L. Shroyer, J. N. Moum, and T. F. Duda, 2012: The unpredictable nature of internal tides on continental shelves. *J. Phys. Oceanogr.*, **42**, 1981–2000, https://doi.org/10.1175/JPO-D-12-028.1.

Perlin, A., J. N. Moum, J. Klymak, M. D. Levine, T. Boyd, and P. M. Kosro, 2005: A modified law-of-the-wall applied to oceanic bottom boundary layers. *J. Geophys. Res.*, **110**, C10S10, https://doi.org/10.1029/2004JC002310.

Pomar, L., M. Morsilli, P. Hallock, and B. Bádenas, 2012: Internal waves, an under-explored source of turbulence events in the sedimentary record. *Earth-Sci. Rev.*, **111**, 56–81, https://doi.org/10.1016/j.earscirev.2011.12.005.

Rippeth, T. P., and M. E. Inall, 2002: Observations of the internal tide and associated mixing across the Malin Shelf. *J. Geophys. Res.*, **107**, 3028, https://doi.org/10.1029/2000JC000761.

Sandstrom, H., and J. Elliott, 1984: Internal tide and solitons on the Scotian Shelf: A nutrient pump at work. *J. Geophys. Res.*, **89**, 6415–6426, https://doi.org/10.1029/JC089iC04p06415.

——, and N. Oakey, 1995: Dissipation in internal tides and solitary waves. *J. Phys. Oceanogr.*, **25**, 604–614, https://doi.org/10.1175/1520-0485(1995)025<0604:DIITAS>2.0.CO;2.

Scotti, A., and J. Pineda, 2007: Plankton accumulation and transport in propagating nonlinear internal fronts. *J. Mar. Res.*, **65**, 117–145, https://doi.org/10.1357/002224007780388702.

——, R. C. Beardsley, B. Butman, and J. Pineda, 2008: Shoaling of nonlinear internal waves in Massachusetts Bay. *J. Geophys. Res.*, **113**, C08031, https://doi.org/10.1029/2008JC004726.

Sharples, J., and Coauthors, 2007: Spring-neap modulation of internal tide mixing and vertical nitrate fluxes at a shelf edge in summer. *Limnol. Oceanogr.*, **52**, 1735–1747, https://doi.org/10.4319/lo.2007.52.5.1735.

——, and J. R. Zeldis, 2019: Variability of internal tide energy, mixing and nitrate fluxes in response to changes in stratification on the northeast New Zealand continental shelf. *N. Z. J. Mar. Freshwater Res.*, **55**, 94–111, https://doi.org/10.1080/00288330.2019.1705357.

——, C. M. Moore, and E. R. Abraham, 2001: Internal tide dissipation, mixing, and vertical nitrate flux at the shelf edge of NE New Zealand. *J. Geophys. Res.*, **106**, 14 069–14 081, https://doi.org/10.1029/2000JC000604.

Sherwin, T., 1988: Analysis of an internal tide observed on the Malin Shelf, north of Ireland. *J. Phys. Oceanogr.*, **18**, 1035–1050, https://doi.org/10.1175/1520-0485(1988)018<1035:AOAITO>2.0.CO;2.

Shroyer, E., J. Moum, and J. Nash, 2010a: Energy transformations and dissipation of nonlinear internal waves over New Jersey's continental shelf. *Nonlinear Processes Geophys.*, **17**, 345–360, https://doi.org/10.5194/npg-17-345-2010.

Shroyer, E. L., J. N. Moum, and J. D. Nash, 2010b: Vertical heat flux and lateral mass transport in nonlinear internal waves. *Geophys. Res. Lett.*, **37**, L08601, https://doi.org/10.1029/2010GL042715.

——, ——, and ——, 2011: Nonlinear internal waves over New Jersey's continental shelf. *J. Geophys. Res.*, **116**, C03022, https://doi.org/10.1029/2010JC006332.

Spydell, M. S., F. Feddersen, and J. Macmahan, 2019: The effect of drifter GPS errors on estimates of submesoscale vorticity. *J. Atmos. Oceanic Technol.*, **36**, 2101–2119, https://doi.org/10.1175/JTECH-D-19-0108.1.

Stastna, M., and K. G. Lamb, 2002: Large fully nonlinear internal solitary waves: The effect of background current. *Phys. Fluids*, **14**, 2987–2999, https://doi.org/10.1063/1.1496510.

Suanda, S. H., and Coauthors, 2016: Wind relaxation and a coastal buoyant plume north of Pt. Conception, CA: Observations, simulations, and scalings. *J. Geophys. Res. Oceans*, **121**, 7455–7475, https://doi.org/10.1002/2016JC011919.

——, F. Feddersen, and N. Kumar, 2017: The effect of barotropic and baroclinic tides on coastal stratification and mixing. *J. Geophys. Res. Oceans*, **122**, 10–156, https://doi.org/10.1002/2017JC013379.

Thornton, E. B., and R. Guza, 1983: Transformation of wave height distribution. *J. Geophys. Res.*, **88**, 5925–5938, https://doi.org/10.1029/JC088iC10p05925.

Venayagamoorthy, S. K., and O. B. Fringer, 2007: On the formation and propagation of nonlinear internal boluses across a shelf break. *J. Fluid Mech.*, **577**, 137–159, https://doi.org/10.1017/S0022112007004624.

Vlasenko, V., and K. Hutter, 2002: Numerical experiments on the breaking of solitary internal wavesover a slope–shelf topography. *J. Phys. Oceanogr.*, **32**, 1779–1793, https://doi.org/10.1175/1520-0485(2002)032<1779:NEOTBO>2.0.CO;2.

Walter, R. K., E. C. Reid, K. A. Davis, K. J. Armenta, K. Merhoff, and N. J. Nidzieko, 2017: Local diurnal wind-driven variability and upwelling in a small coastal embayment. *J. Geophys. Res. Oceans*, **122**, 955–972, https://doi.org/10.1002/2016JC012466.

Washburn, L., M. R. Fewings, C. Melton, and C. Gotschalk, 2011: The propagating response of coastal circulation due to wind relaxations along the central California coast. *J. Geophys. Res.*, **116**, C12028, https://doi.org/10.1029/2011JC007502.